

Supporting Information for ”Removing climatic overprints in sedimentary cosmogenic beryllium records: Potentials and limits”

Tatiana Savranskaia^{1‡}, Ramon Egl^{2,3}, Quentin Simon⁴, Jean-Pierre Valet²,
Franck Bassinot⁵, Nicolas Thouveny⁴

¹GeoForschungsZentrum (GFZ) Potsdam, Telegrafenberg, 14473 Potsdam, Germany

²Université de Paris, Institut de physique du globe de Paris, CNRS, F-75005 Paris, France

³Department of Geophysics, GeoSphere Austria, 1190, Vienna, Austria

⁴CEREGE UM34, Aix Marseille Univ, CNRS, IRD, INRAE, Coll France, 13545, Aix en Provence, France

⁵Laboratoire des Sciences Du Climat et de l’Environnement (CEA-CNRS-UVSQ), Domaine Du
CNRS,91198, Gif-sur-Yvette, France

Contents of this file

1. **Text S1.** Description of Rock magnetic measurements.
2. **Text S2.** An age-depth model construction.
3. **Table S1.** Pearson correlation coefficients r between Be isotopes and environmental proxies in core MD95-2016.
4. **Table S2.** Pearson correlation coefficients r between the first six principal components and Be records, $\delta^{18}\text{O}$, XRF elemental ratios, and magnetic susceptibility.
5. **Table S3.** Temporal occurrence of recognized geomagnetic events between $^{10}\text{Be}_{\text{geo}}$, SINT-2000, and PISO-1500.
6. **Figure S1.** Rock magnetic parameters and $\delta^{18}\text{O}$ variations.
7. **Figure S2.** Relative paleointensity and authigenic ^{10}Be from core MD95-2016 compared with SINT-2000 converted to the global beryllium production rate P/P_0 .
8. **Figures S3.** Age model of the MD95-2016 sediment core and comparison of the $\delta^{18}\text{O}$ record in the same core with the probabilistic stack HMM.
9. **Figures S4.** Relative contribution (%) of principal components and estimated confidence intervals.
10. **Figures S5.** PCA results for higher order principal components.

[‡]Present Address: Department of Earth and Environmental Sciences, Ludwig Maximilians University, Theresienstr 41, 80333 Munich, Germany

11. **Figures S6.** Records of the Laschamps and Icelandic Basin geomagnetic excursions by $^{10}\text{Be}_{\text{geo}}$ and by SINT-2000 converted to P/P_0 .
12. **Figures S7.** Original and time-adjusted $^{10}\text{Be}_{\text{geo}}$ records, converted to beryllium production rate P/P_0 and compared with SINT-2000.
13. **Figures S8.** Relation between m/m_0 obtained from the SINT-2000 RPI stack and P/P_0 obtained from $^{10}\text{Be}_{\text{geo}}$ and $^{10}\text{Be}_{\text{geo}}$, adjusted for the temporal offsets during the Laschamps and Icelandic Basin geomagnetic excursions.
14. **Figures S9.** Results of PCA with normalized ^{10}Be with χ .
15. **Figures S10.** Comparison of ^9Be from MD95-2016 with Deep North Atlantic and HMM $\delta^{18}\text{O}$ stacks.

Text S1. Magnetic measurements and relative paleointensity

Natural remanent magnetization (NRM), anhysteretic remanent magnetization (ARM) and low-field magnetic susceptibility (χ) of core MD95-2016 were measured on U-channels and discrete samples using a 2G Enterprises cryogenic magnetometer and an Agico KLY-3 susceptibility meter inside the shielded room of the paleomagnetic laboratory at the Institut de Physique du Globe de Paris. In total, 29 meters of U-channels sections and 1071 single samples taken every 2 cm using $\sim 8 \text{ cm}^3$ plastic cubes. Samples and U-channels were step-wise demagnetized in alternating fields (AF) of peak amplitudes comprised between 10 to 90 mT. Viscous overprints are generally limited to the 0-10 mT range. Characteristic NRM directions were determined from the 50–80 mT demagnetization interval for the discrete samples and from 30–90 mT interval for U-channels. Characteristic direction with a mean angular deviation in excess of 10° were disregarded.

The anhysteretic remanent magnetisation (ARM) imparted in a 80 mT peak AF field and 0.05 mT DC bias field was demagnetized at the same steps as the NRM. Proxies for the concentration of low-coercivity magnetic minerals and their finer fraction are given by ARM and χ , respectively. ARM/χ is a proxy for magnetic grain size (Maher, 1988; Banerjee et al., 1981). Variations of this parameter (Figure S3) by up to a factor of four hamper RPI calculations based on the normalization of NRM measurements with ARM or χ . Changes in magnetic concentration and grain size are strongly affected by climatic stages, as seen by the comparison of magnetic proxies with $\delta^{18}\text{O}$ (Figure S3). The concentration and size of magnetic minerals is maximal during cold stages and minimal during interglacials. Concentration variations are mainly driven by massive discharge of massive glacial detritus with coarser grain size from melted ice masses and by carbonate dilution during interglacial (Robinson et al., 1995).

Relative paleointensity (RPI) was estimated as mean value of NRM/ARM ratio over the 30–90 mT range of AF demagnetization (Figure S3). Almost identical RPI variations are obtained with the pseudo-Thellier method (Tauxe et al., 1995), which relies on NRM-ARM demagnetization slopes. This confirms the stability of NRM. However, NRM normalization fails, due to the strong magnetic grain size variability shown by ARM/χ .

Text S2. An age-depth model construction

The standard approach for depth-age model construction relies on fitting the $\delta^{18}\text{O}$ record to a reference, commonly a stack curve, and following astronomical tuning if more precise orbitally-paced signals are available. The global benthic $\delta^{18}\text{O}$ stack LR04 (Lisiecki & Raymo, 2005) is the most widely used target curve because it integrates 57 globally distributed benthic records spanning the past 5.3 Ma. The HMM stack used here is a recent update of LR04 based on a hidden Markov model that includes a larger number of records (Ahn et al., 2017). Tuning a single-location $\delta^{18}\text{O}$ record to the global $\delta^{18}\text{O}$ stack might bias the age-depth model due to the incomplete global synchronisation of $\delta^{18}\text{O}$ variability (Labeyrie et al., 2005; Waelbroeck et al., 2011). Age lags were addressed by constructing regional benthic $\delta^{18}\text{O}$ stacks covering the past 150 ka (Lisiecki & Stern, 2016). Regional stacks enable a better synchronization of geographically close records.

The age model was constructed in four steps:

1. **Age tie points.** Define age tie points by matching the peaks of Ice Rafted Debris (IRD) events in core MD95-2016 and U1308 (Hodell et al., 2008), using Si/Sr and Zr/Sr as IRD proxies (Figure S1). The choice of U1308 as a target core is determined by its accurate age model being constrained by radiocarbon dates and oxygen isotopes stratigraphy with Greenland ice cores (Svensson et al., 2006) for the last 42 ka, and with the benthic stack LR04 prior to 60 ka. Planktonic $\delta^{18}\text{O}$ records can be affected by significant age offsets caused by foraminifera dissolution (e.g., Barker et al., 2007), and size segregation (Savranskaia et al., 2022) effects.
2. **Age offset corrections.** Define additional tie points by matching the ^9Be record of MD95-2016 with the Deep North Atlantic (DNA) $\delta^{18}\text{O}$ stack (Lisiecki & Stern, 2016) (Figure S10). ^9Be is a valid substitute for $\delta^{18}\text{O}$ at this high-latitude site, owing to its strong association with glacial-interglacial cycles and the relatively short residence time in the Atlantic Ocean (von Blanckenburg & O’nions, 1999).
3. **Model correction for the upper part.** Alignment the upper part of the MD95-2016 $\delta^{18}\text{O}$ record with the DNA $\delta^{18}\text{O}$ age model. Due to the limited DNA age coverage prior to 0–135 ka, the older part of sedimentary record was matched with the HMM stack using the software package BIGMACS, which is based on the Bayesian Inference Gaussian Process regression (Lee et al., 2022).

4. **Check accuracy.** Evaluate the accuracy of correlations using the BIGMACS algorithm by comparing the MD95-2016 record with the planktic $\delta^{18}\text{O}$ variations from the neighbour core ODP982 (57°30.8'N, 152°55.5'W) on its independent age scale (Jansen et al., 1996).

References

- Ahn, S., Khider, D., Lisiecki, L. E., & Lawrence, C. E. (2017). A probabilistic Pliocene–Pleistocene stack of benthic $\delta^{18}\text{O}$ using a profile hidden Markov model. *Dynamics and Statistics of the Climate System*, 2(1), dx002.
- Banerjee, S. K., King, J., & Marvin, J. (1981). A rapid method for magnetic granulometry with applications to environmental studies. *Geophysical Research Letters*, 8(4), 333–336.
- Barker, S., Broecker, W., Clark, E., & Hajdas, I. (2007). Radiocarbon age offsets of foraminifera resulting from differential dissolution and fragmentation within the sedimentary bioturbated zone. *Paleoceanography*, 22(2).
- Channell, J. E., Singer, B. S., & Jicha, B. R. (2020). Timing of quaternary geomagnetic reversals and excursions in volcanic and sedimentary archives. *Quaternary Science Reviews*, 228, 106114.
- Coe, R. S., Grommé, S., & Mankinen, E. A. (1978). Geomagnetic paleointensities from radiocarbon-dated lava flows on Hawaii and the question of the Pacific nondipole low. *Journal of Geophysical Research: Solid Earth*, 83(B4), 1740–1756.
- Herbert, T. D., Lawrence, K. T., Tzanova, A., Peterson, L. C., Caballero-Gill, R., & Kelly, C. S. (2016). Late Miocene global cooling and the rise of modern ecosystems. *Nature Geoscience*, 9(11), 843–847.
- Herrero-Bervera, E., Hellsley, C., Sarna-Wojcicki, A., Lajoie, K., Meyer, C., McWilliams, M., ... Liddicoat, J. (1994). Age and correlation of a paleomagnetic episode in the western United States by $^{40}\text{Ar}/^{39}\text{Ar}$ dating and tephrochronology: The Jamaica, Blake, or a new polarity episode? *Journal of Geophysical Research: Solid Earth*, 99(B12), 24091–24103.
- Hodell, D. A., Channell, J. E., Curtis, J. H., Romero, O. E., & Röhl, U. (2008). Onset of “Hudson Strait” Heinrich events in the eastern North Atlantic at the end of the middle Pleistocene transition (640 ka)? *Paleoceanography*, 23(4).
- Jansen, E., Raymo, M., Blum, P., et al. (1996). 1. Leg 162: new frontiers on past climates. In *Proceedings ODP, Initial Reports* (Vol. 162, pp. 5–20).
- Labeyrie, L., Waelbroeck, C., Cortijo, E., Michel, E., & Duplessy, J.-C. (2005). Changes in deep water hydrology during the Last Deglaciation. *Comptes Rendus Geoscience*,

337(10-11), 919–927.

- Laj, C., & Channell, J. E. (2007). Geomagnetic excursions. *Geomagnetism*, 5, 373–416.
- Lanphere, M. A. (2000). Comparison of conventional K–Ar and $^{40}\text{Ar}/^{39}\text{Ar}$ dating of young mafic volcanic rocks. *Quaternary Research*, 53(3), 294–301.
- Lee, T., Rand, D., Lisiecki, L. E., Gebbie, G., & Lawrence, C. E. (2022). Bayesian age models and stacks: Combining age inferences from radiocarbon and benthic $\delta^{18}\text{O}$ stratigraphic alignment. *EGU sphere*, 2022, 1–29.
- Lisiecki, L. E., & Raymo, M. E. (2005). A Pliocene–Pleistocene stack of 57 globally distributed benthic $\delta^{18}\text{O}$ records. *Paleoceanography*, 20(1).
- Lisiecki, L. E., & Stern, J. V. (2016). Regional and global benthic $\delta^{18}\text{O}$ stacks for the last glacial cycle. *Paleoceanography*, 31(10), 1368–1394.
- Liu, J., Nowaczyk, N. R., Frank, U., & Arz, H. W. (2018). A 20–15 ka high-resolution paleomagnetic secular variation record from Black Sea sediments—no evidence for the ‘Hilina Pali excursion’? *Earth and Planetary Science Letters*, 492, 174–185.
- Lund, S. (2022). A summary of paleomagnetic secular variation and excursions for the last 380 ky of the Brunhes normal polarity Chron. *Physics of the Earth and Planetary Interiors*, 333, 106923.
- Lund, S., Stoner, J. S., Channell, J. E., & Acton, G. (2006). A summary of Brunhes paleomagnetic field variability recorded in Ocean Drilling Program cores. *Physics of the Earth and Planetary Interiors*, 156(3-4), 194–204.
- Maher, B. A. (1988). Magnetic properties of some synthetic sub-micron magnetites. *Geophysical Journal International*, 94(1), 83–96.
- Robinson, S. G., Maslin, M. A., & McCave, I. N. (1995). Magnetic susceptibility variations in Upper Pleistocene deep-sea sediments of the NE Atlantic: Implications for ice rafting and paleocirculation at the last glacial maximum. *Paleoceanography*, 10(2), 221–250.
- Savranskaia, T., Egli, R., & Valet, J.-P. (2022). Multiscale Brazil nut effects in bioturbated sediment. *Scientific reports*, 12(1), 11450.
- Simon, Q., Thouveny, N., Bourlès, D. L., Valet, J.-P., Bassinot, F., Ménébréaz, L., . . . Beaufort, L. (2016). Authigenic $^{10}\text{Be}/^9\text{Be}$ ratio signatures of the cosmogenic nuclide production linked to geomagnetic dipole moment variation since the Brunhes/Matuyama boundary. *Journal of Geophysical Research: Solid Earth*, 121(11), 7716–7741.
- Singer, B., Relle, M., Hoffman, K., Battle, A., Laj, C., Guillou, H., & Carracedo, J. (2002). Ar/Ar ages from transitionally magnetized lavas on La Palma, Canary Islands, and the ge-

- omagnetic instability timescale. *Journal of Geophysical Research: Solid Earth*, *107*(B11), EPM-7.
- Singer, B. S., Guillou, H., Jicha, B. R., Laj, C., Kissel, C., Beard, B. L., & Johnson, C. M. (2009). $^{40}\text{Ar}/^{39}\text{Ar}$, K-Ar and ^{230}Th - ^{238}U dating of the Laschamp excursion: a radioisotopic tie-point for ice core and climate chronologies. *Earth and Planetary Science Letters*, *286*(1-2), 80-88.
- Singer, B. S., Guillou, H., Jicha, B. R., Zanella, E., & Camps, P. (2014). Refining the quaternary geomagnetic instability time scale (GITS): Lava flow recordings of the Blake and Post-Blake excursions. *Quaternary Geochronology*, *21*, 16-28.
- Singer, B. S., Jicha, B. R., He, H., & Zhu, R. (2014). Geomagnetic field excursion recorded 17 ka at Tianchi Volcano, China: New $^{40}\text{Ar}/^{39}\text{Ar}$ age and significance. *Geophysical Research Letters*, *41*(8), 2794-2802.
- Svensson, A., Andersen, K. K., Bigler, M., Clausen, H. B., Dahl-Jensen, D., Davies, S. M., ... others (2006). The greenland ice core chronology 2005, 15-42 ka. part 2: comparison to other records. *Quaternary Science Reviews*, *25*(23-24), 3258-3267.
- Tauxe, L., Pick, T., & Kok, Y. (1995). Relative paleointensity in sediments: A pseudo-Thellier approach. *Geophysical Research Letters*, *22*(21), 2885-2888.
- Thouveny, N., Bourlès, D. L., Saracco, G., Carcaillet, J. T., & Bassinot, F. (2008). Paleoclimatic context of geomagnetic dipole lows and excursions in the Brunhes, clue for an orbital influence on the geodynamo? *Earth and Planetary Science Letters*, *275*(3-4), 269-284.
- Thouveny, N., Carcaillet, J., Moreno, E., Leduc, G., & Nérini, D. (2004). Geomagnetic moment variation and paleomagnetic excursions since 400 kyr BP: a stacked record from sedimentary sequences of the Portuguese margin. *Earth and Planetary Science Letters*, *219*(3-4), 377-396.
- von Blanckenburg, F., & O'niions, R. (1999). Response of beryllium and radiogenic isotope ratios in Northern Atlantic Deep Water to the onset of northern hemisphere glaciation. *Earth and planetary science letters*, *167*(3-4), 175-182.
- Waelbroeck, C., Skinner, L. C., Labeyrie, L., Duplessy, J.-C., Michel, E., Vazquez Riveiros, N., ... Dewilde, F. (2011). The timing of deglacial circulation changes in the Atlantic. *Paleoceanography*, *26*(3).

	$\delta^{18}\text{O}$	^9Be	^{10}Be	$^{10}\text{Be}/^9\text{Be}$
$\delta^{18}\text{O}$	1	+0.44	-0.09	-0.37
^9Be	+0.44	1	+0.32	-0.42
^{10}Be	-0.09	+0.32	1	+0.66
$^{10}\text{Be}/^9\text{Be}$	-0.37	-0.42	+0.66	1
χ	+0.12	-0.09	-0.32	+0.33
Si/Sr	+0.31	+0.47	-0.13	-0.44
Ca/Sr	-0.37	-0.38	-0.008	+0.27
Sr/Rb	-0.56	-0.66	-0.08	+0.53
Ti/Ca	+0.52	+0.65	-0.006	-0.47
Ti/K	-0.31	-0.12	-0.24	+0.25
Zr/Sr	-0.49	-0.59	-0.12	-0.53

Table S1: Pearson correlation coefficients r between Be isotopes and environmental proxies in core MD95-2016.

	$\delta^{18}\text{O}$	^9Be	^{10}Be	χ	Si/Sr	Ca/Sr	Sr/Rb	Ti/Ca	Ti/K	Zr/Sr
PC₁	+0.653	+0.769	-0.020	-0.306	+0.669	-0.682	-0.965	+0.934	-0.343	+0.936
PC₂	+0.030	-0.258	-0.783	-0.669	+0.189	+0.229	+0.031	-0.175	-0.639	-0.002
PC₃	+0.180	+0.390	+0.486	-0.107	+0.312	+0.502	-0.019	-0.214	-0.471	-0.155
PC₄	+0.144	-0.078	-0.313	0.623	0.409	0.327	-0.044	0.040	-0.039	0.113
PC₅	0.668	-0.052	-0.038	0.136	-0.364	-0.207	0.083	-0.118	-0.213	-0.155
PC₆	0.213	0.209	-0.135	-0.164	0.001	0.194	0.087	0.045	0.431	-0.049

Table S2: Pearson correlation coefficients r between the first six principal components and Be records, $\delta^{18}\text{O}$, XRF elemental ratios, and magnetic susceptibility.

Nº	Recognized excursion	Age interval (ka)	$^{10}\text{Be}_{geo}$	SINT-2000	PISO-1500	Reference
1	Hilina Pali	17±3	15-18	-	19	1,15
2	Laschamps	40 ±1	36-39	38-41	41	2,3
3	Norwegian Greenland Sea	62 ±2	63-65	65	64	3,14
4	Fram St./Post-blake	98±7	101	99	99	4,5,12
5	Blake	120±12	113-117	114	120	5,6
6	Icelandic Basin	188±2	186-192	190	195	5,11
7	Pringle falls	212±13	209	213	213-220	6,9
8	Portuguese Margin	286-290	283	283	286	6,10
9	Calabrian Ridge	315-325	315	317	321	5,11
10	Biwa III	368-402	390	390	401	5
11	Calabrian Ridge II	515-528	517	533	526	5,11,14
12	Big Lost	558±14	552	555	560	6,13
13	La Palma	575±8	580-590	590	589	6,8

Table S3: Temporal occurrence of recognized geomagnetic events between $^{10}\text{Be}_{geo}$, SINT-2000, and PISO-1500. 1. B. S. Singer, Jicha, et al. (2014); 2. B. S. Singer et al. (2009), 3. Lund et al. (2006), 4. B. S. Singer, Guillou, et al. (2014), 5. Laj & Channell (2007), 6. Channell et al. (2020), 7. Coe et al. (1978), 8. B. Singer et al. (2002), 9. Herrero-Bervera et al. (1994), 10. Thouveny et al. (2004), 11. Thouveny et al. (2008), 12. Lund (2022), 13. Lanphere (2000), 14. Simon et al. (2016), 15. Liu et al. (2018)

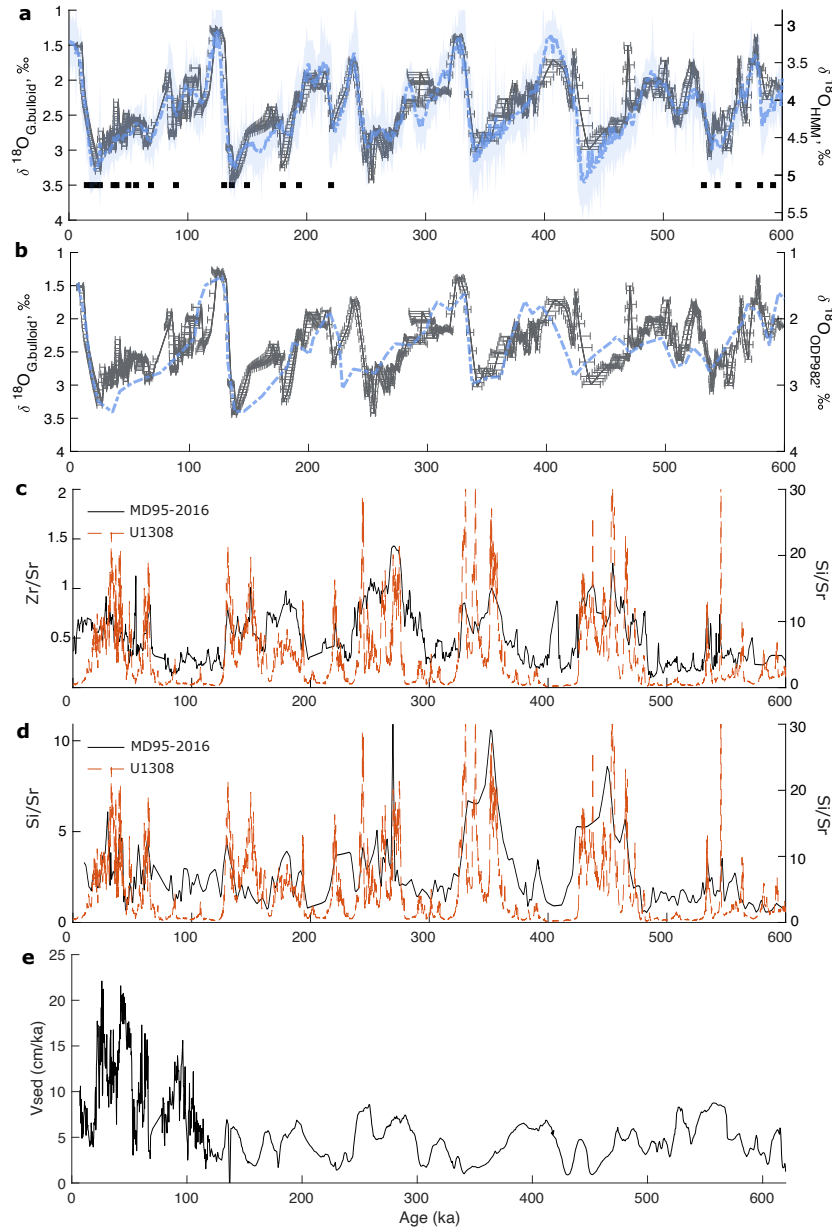


Figure S1: (a) Planktonic $\delta^{18}\text{O}$ record from MD95-2016 (solid black line, left scale) compared to the global benthic $\delta^{18}\text{O}$ probabilistic stack HHM (Ahn et al., 2017) (dashed blue line with 95% confidence interval). The age uncertainties for MD95-2016 are obtained with the BIGMACS emission model (Lee et al., 2022). Black squares represent tie points used to convert depth to age scale. (b) Planktonic $\delta^{18}\text{O}$ records from MD95-2016 and from the neighbour core ODP982 (Jansen et al., 1996) on their own age scales. Comparison of XRF Si/Sr signal from MD95-2016 (black solid line) with (c) Zr/Sr and (d) (Si/Sr) from North Atlantic site U1308 (Hodell et al., 2008). (e) Sedimentation rate associated with age-depth model for sedimentary core MD95-2016.

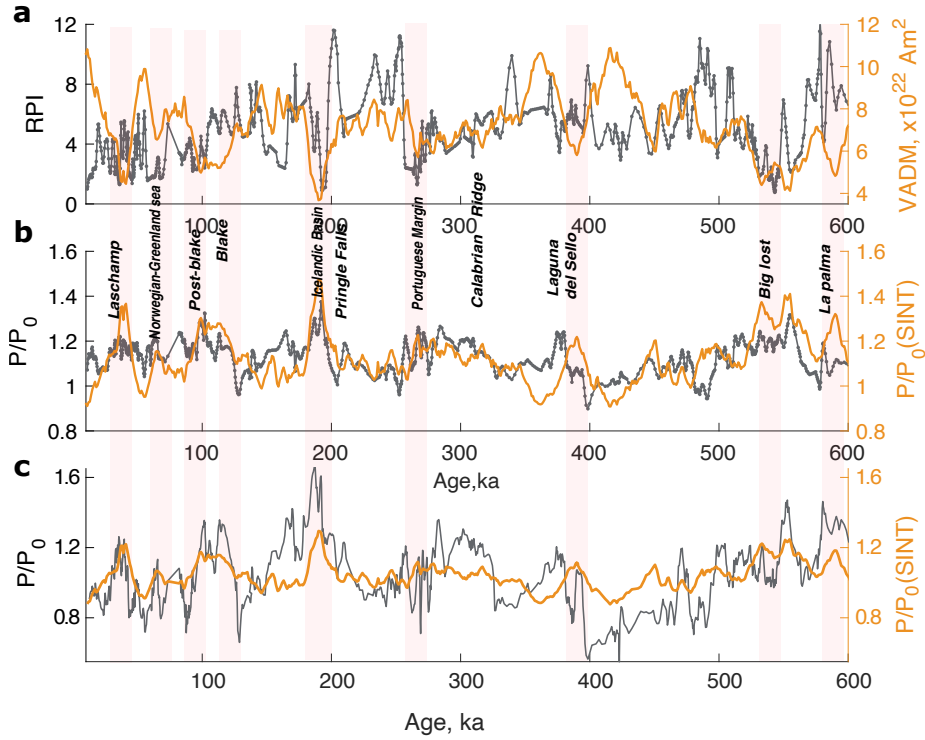


Figure S2: (a) Relative paleointensity (mean NRM/ARM ratio over the 30-80 mT AF demagnetisation range) obtained from u-channel measurements, compared with SINT-2000 VADM record. The RPI values were scaled to VADM (SINT-2000) for better comparison; (b) $^{10}\text{Be}_{\text{geo}}$ converted to normalized beryllium production rate P/P_0 , obtained from a PCA solution with RPI and ARM included into the dataset; (c) same as (b), but RPI and ARM have not been included into the dataset. Vertical bands highlight recognized geomagnetic excursions (Table S3) over the past 600 ka.

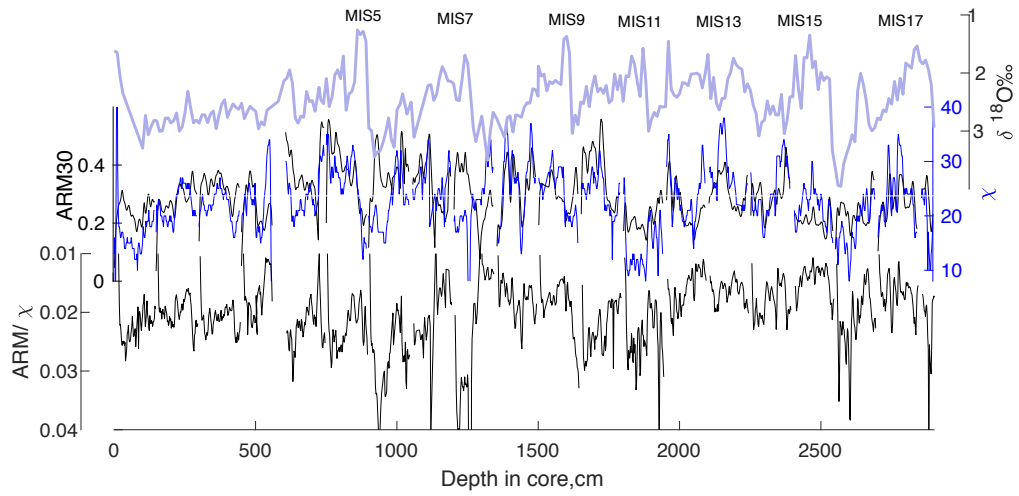


Figure S3: Normalizers of Natural Remanent Magnetisation - ARM measured after 30 mT peak AF demagnetization (ARM30) and proxy of magnetic grain size variations ARM/ χ together with $\delta^{18}\text{O}$ from planktonik foraminifera, measured in MD95-2016 sediments.

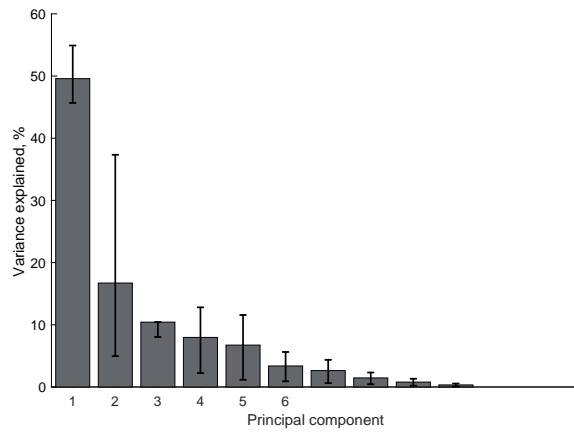


Figure S4: Explained variance (%) by principal components of MD95-2016 within estimated confidence interval.

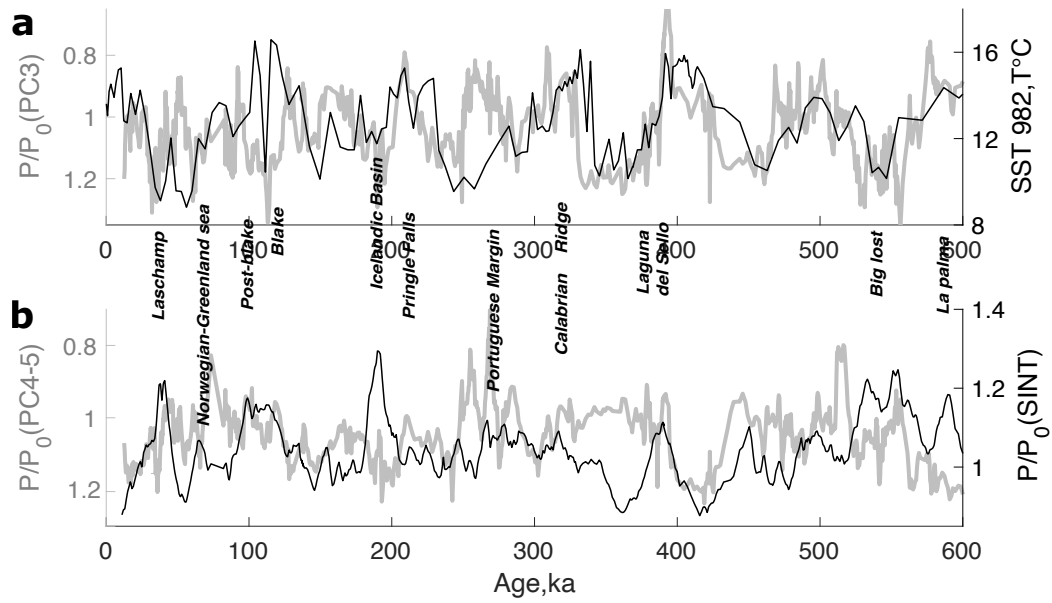


Figure S5: Results of PCA (higher order components). **(a)** PC3 converted to global production P/P_0 (gray line) and Sea Surface Temperature from neighbour site ODP982 (Herbert et al., 2016); **(b)** Sum of PC4 and PC5 (gray line) and RPI stack SINT-2000 (black) converted to P/P_0 .

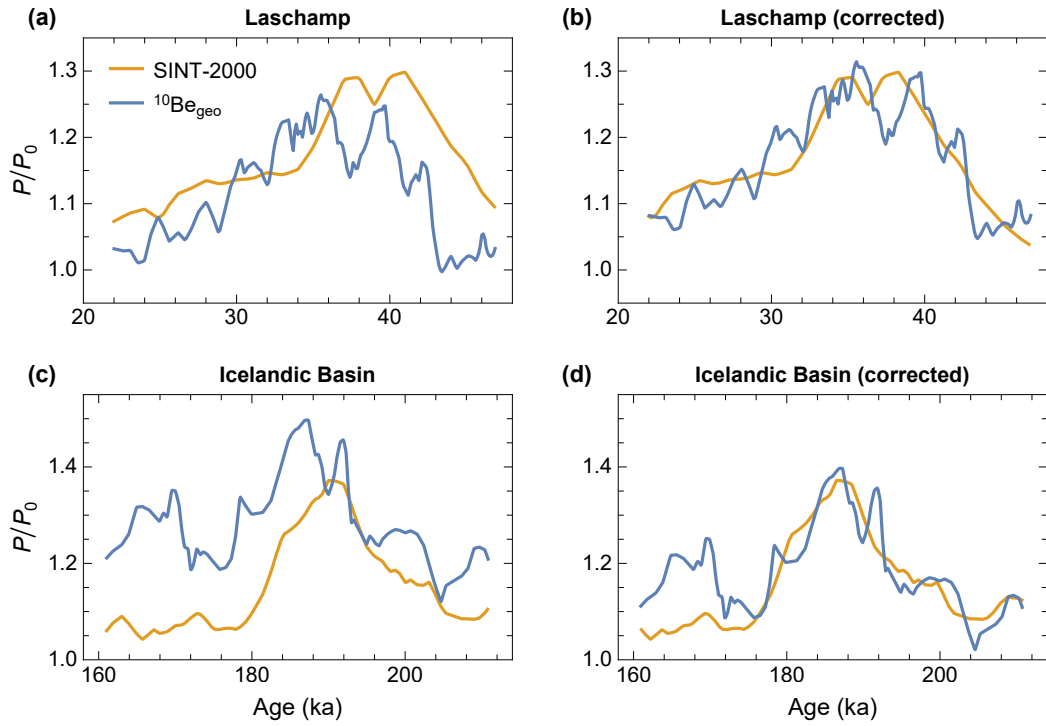


Figure S6: Records of the Laschamps (a,b) and Icelandic Basin (c,d) geomagnetic excursions by $^{10}\text{Be}_{\text{geo}}$ and by SINT-2000 converted to P/P_0 . Left and right plots show the original and the corrected $^{10}\text{Be}_{\text{geo}}$ record, respectively. Corrected records have been obtained through horizontal and vertical shifts, until the mean squared differences with SINT-2000 were minimized. The corresponding age offsets in (b) and (c) are 2.7 and 3.5 ka, respectively.

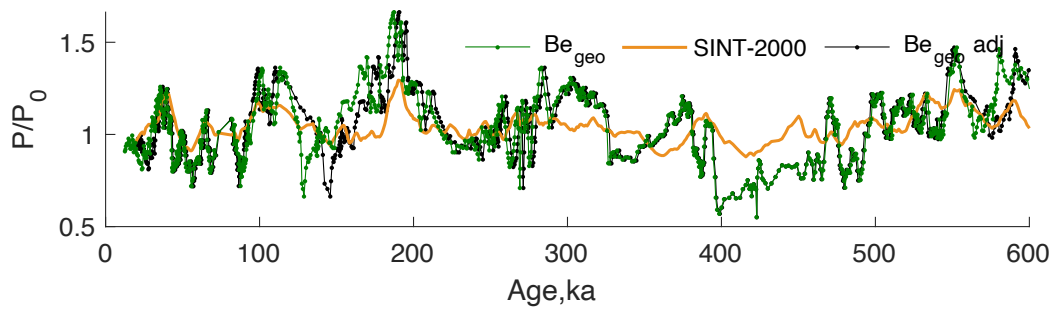


Figure S7: SINT-2000 together with original (green curve) and adjusted (black) for the time delay $^{10}\text{Be}_{\text{geo}}$ records, converted to the beryllium production rate P/P_0 .

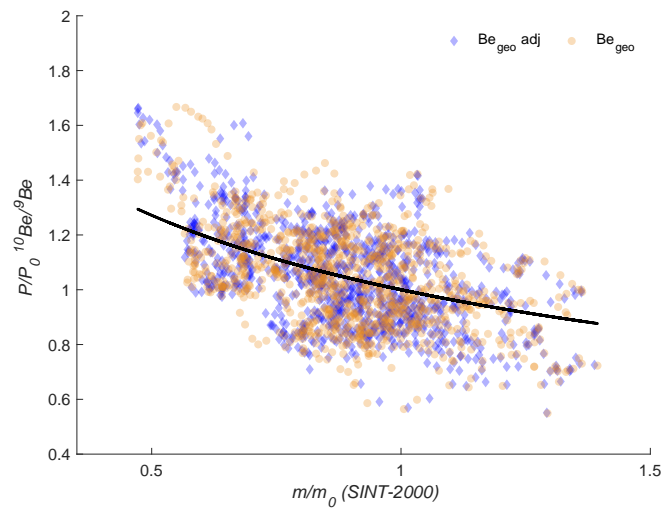


Figure S8: Relation between m/m_0 obtained from the SINT-2000 RPI stack and P/P_0 obtained from $^{10}\text{Be}_{\text{geo}}$ (orange circles) and from $^{10}\text{Be}_{\text{geo}}$ after removing the temporal offsets (Figure S7) related to Group 3 artifacts (blue diamonds).

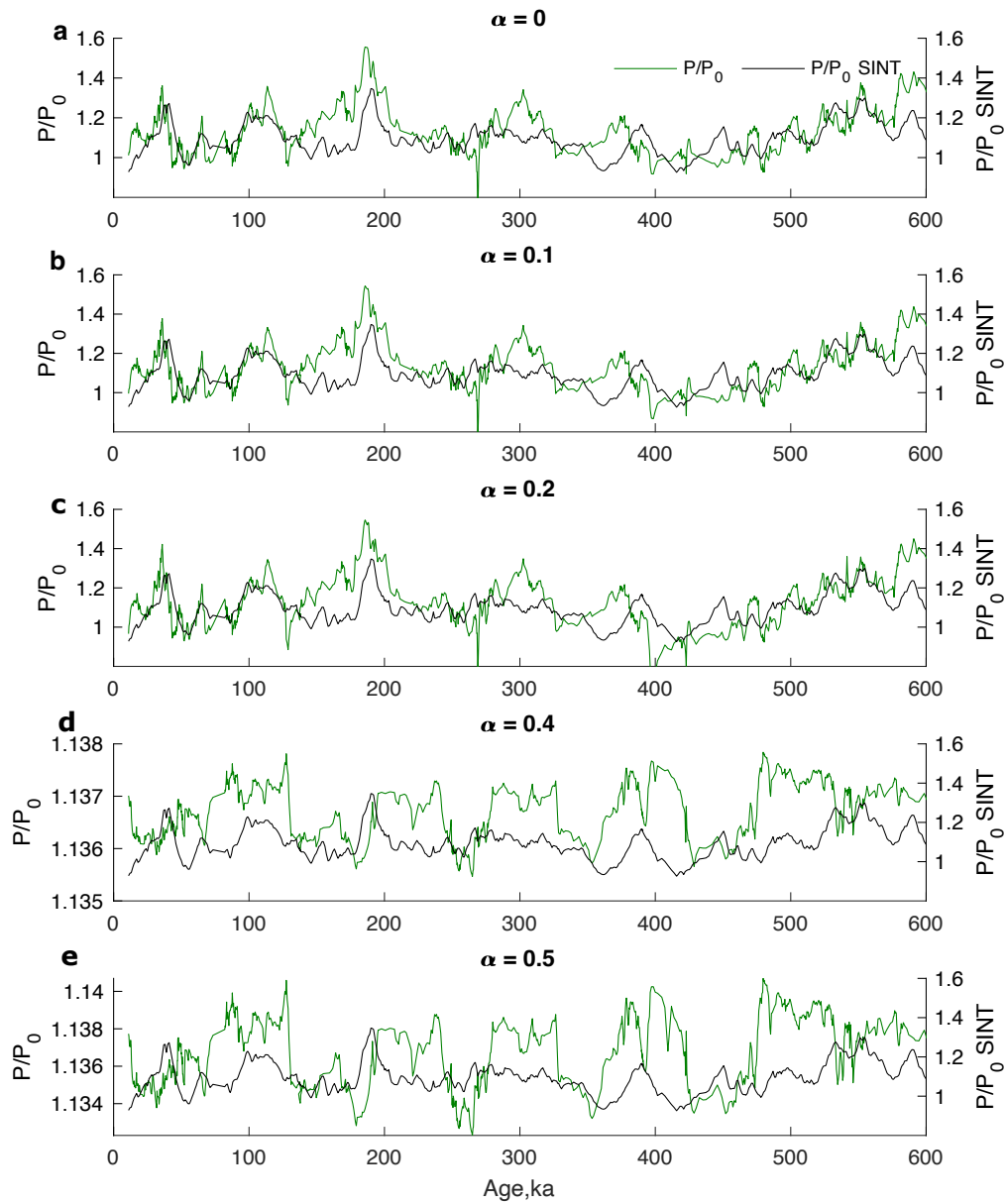


Figure S9: Results of PCA obtained with ^{10}Be normalized by $\alpha * \chi$, where α an empirical factor and χ is magnetic susceptibility. Cases **a–e** correspond to the indicated α above each panel.

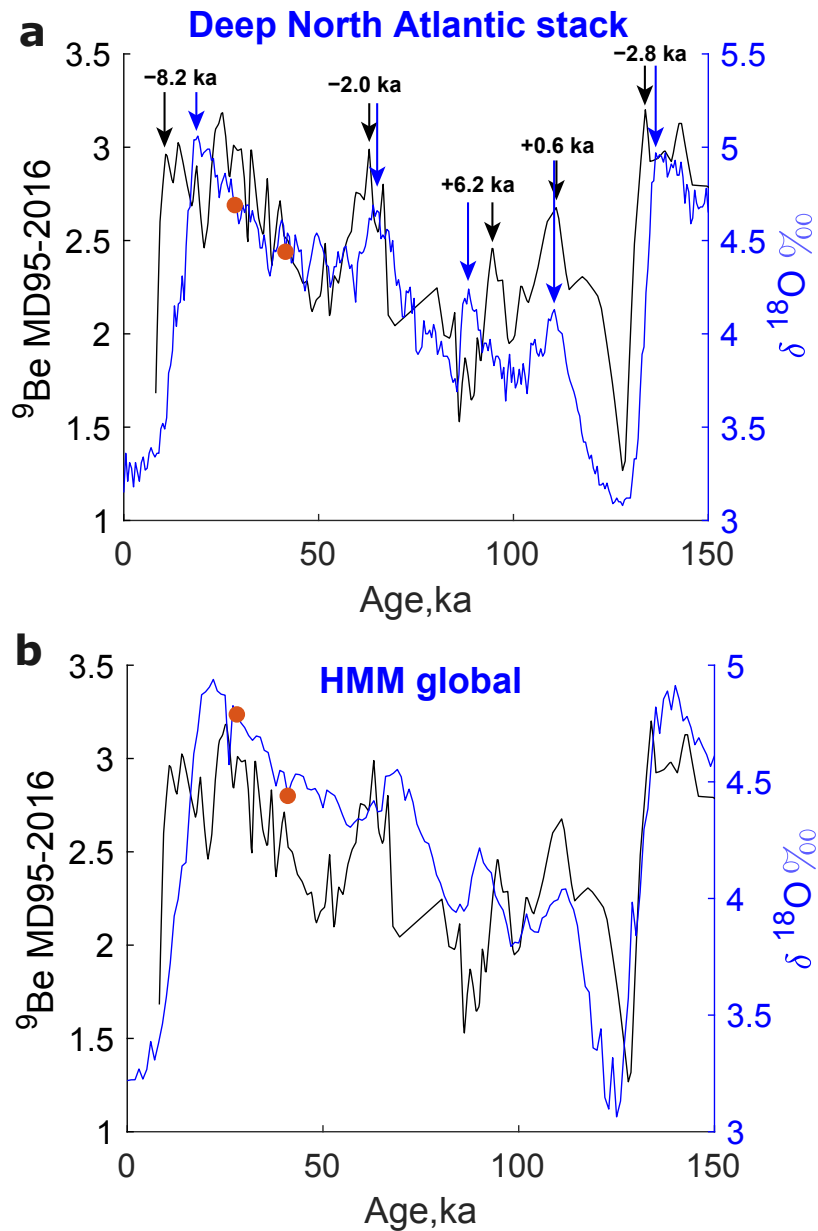


Figure S10: Comparison of ${}^9\text{Be}$ from MD95-2016 with (a) the Deep North Atlantic $\delta^{18}\text{O}$ stack (Lisiecki & Stern, 2016) and (b) the HMM $\delta^{18}\text{O}$ stack (Ahn et al., 2017). The red filled circles mark the 28 ka and 41ka ages of the Mono Lake/Auckland and Laschamps excursions, respectively. The black and blue arrows are used to highlight the offset between two signals. The $\delta^{18}\text{O}$ record is delayed with respect to ${}^9\text{Be}$ during the glacial stages, whereas no or positive $\delta^{18}\text{O}$ delay is observed for the interglacial periods.